Geometric Validation of Continuous, Finely Sampled 3-D Reconstructions From aOCT and CT in Upper Airway Models

Hillel B. Price, Julia S. Kimbell, Ruofei Bu, and Amy L. Oldenburg

Abstract— **Identification and treatment of obstructive airway disorders (OADs) are greatly aided by imaging of the geometry of the airway lumen. Anatomical optical coherence tomography (aOCT) is a promising high-speed and minimally invasive endoscopic imaging modality for providing micrometer-resolution scans of the upper airway. Resistance to airflow in OADs is directly caused by the reduction in luminal cross-sectional area (CSA). It is hypothesized that aOCT can produce airway CSA measurements as accurate as that from computed tomography (CT). Scans of machine hollowed cylindrical tubes were used to develop methods for segmentation and measurement of airway lumen in CT and aOCT. Simulated scans of virtual cones were used to validate 3-D resampling and reconstruction methods in aOCT. Then, measurements of two segments of a 3-D printed pediatric airway phantom from aOCT and CT independently were compared to ground truth CSA. In continuous unobstructed regions, the mean CSA difference for each phantom segment was 2.2 ± 3.5 and 1.5 ± 5.3 mm^2 for aOCT, and −3.4 ± 4.3 and −1.9 ± 1.2 mm^2 for CT. Because of the similar magnitude of these differences, these results support the hypotheses and underscore the potential for aOCT as a viable alternative to CT in airway imaging, while offering greater potential to capture respiratory dynamics.**

Index Terms— **Optical coherence tomography, endoscopy, upper airway, segmentation, image reconstruction, computed tomography.**

H. B. Price is with the Department of Physics and Astronomy, The University of North Carolina at Chapel Hill, Chapel Hill, NC 27599-3255 USA (e-mail: hbprice@live.unc.edu).

J. S. Kimbell is with the Department of Otolaryngology/Head and Neck Surgery, School of Medicine, The University of North Carolina at Chapel Hill, Chapel Hill, NC 27599-7070 USA, and also with the Department of Biomedical Engineering, The University of North Carolina at Chapel Hill, Chapel Hill, NC 27599-3216 USA (e-mail: julia_kimbell@med.unc.edu).

R. Bu is with the Department of Biomedical Medical Engineering, The University of North Carolina at Chapel Hill, Chapel Hill, NC 27599-3216 USA (e-mail: ruofei@email.unc.edu).

A. L. Oldenburg is with the Department of Physics and Astronomy, The University of North Carolina at Chapel Hill, Chapel Hill, NC 27599-3255 USA, with the Biomedical Research Imaging Center, The University of North Carolina at Chapel Hill, Chapel Hill, NC 27599-7513 USA, and also with the Department of Biomedical Medical Engineering, The University of North Carolina at Chapel Hill, Chapel Hill, NC 27599-3216 USA (e-mail: aold@physics.unc.edu).

Color versions of one or more of the figures in this paper are available online at http://ieeexplore.ieee.org.

Digital Object Identifier 10.1109/TMI.2018.2876625

I. INTRODUCTION

IMAGING of airway morphological and physiological properties can aid in treatment and studying pathogenesis of obstructive airway disorders (OADs) [1] such as obstructive sleep apnea (OSA) [2], subglottic stenosis (SGS) [3], chronic obstructive pulmonary disease (COPD) [4], and asthma [5]. Airflow is dependent on airway size and shape, and is reduced when the airways are obstructed or restricted. For example, OSA is a condition characterized by intermittent breathing while sleeping because of airway collapse. The gold standard for diagnosis of OSA is polysomnography [6], however polysomnography lacks data on airway structure which may aid in surgical planning. SGS manifests from natural airway responses to events such as intubation, trauma, infections, and lesions which give rise to airway tissue inflammation and fibrosis that compromise airflow [7], [8]. Endoscopy is the gold-standard for studying and diagnosing OADs, but it is semi-quantitative at best and limited to a surface view of airway tissues. Quantitative imaging of the size and shape of the air-tissue interface is needed to build geometric airway models. Such models can guide computational fluid dynamics (CFD) simulations of airflow, which have been used to characterize patients with and without OSA [1], [2] and to predict the response to treatment [9].

Methods such as MRI, CT, and Optical Coherence Tomography (OCT) can provide quantitative measurements and 3D reconstructions of lumen. However MRI and CT have limited spatial and temporal resolution when compared to OCT, making it difficult to accurately capture airway geometry during respiration. Newer and still developing multimodal and deep learning techniques also show promise for virtual reconstruction and fast classification of lumen [10], [11]. OCT can be portable and employed endoscopically from the examination room to capture live micrometer-resolution airway cross-sections with high frame rates (∼10 frames/s), providing medical professionals with rapid and non-invasive static and dynamic [12]–[14] images of the airway wall and underlying tissue layers [4], [15]. Long-range or anatomic OCT (aOCT) is a particular form of OCT developed to offer the greater imaging ranges needed to assess larger luminal spaces such as the upper airway. Several groups have been performing research using aOCT including intraoperative measurements of the airway cross-sectional area after adenotonsillectomy in pediatric patients [16], retrospective prediction of extubation

failure related to SGS in neonates [3], comparing difference in airway size between male and female COPD patients [17], and using aOCT data to build CFD models able to differentiate patients with and without OSA [1].

Often the accuracy of methods for collecting and analyzing quantitative images of lumen are validated and quantified by measurements of phantoms of well-known "ground truth" properties [18]–[21]. The accuracy, however, can be biased by how the phantom's ground truth properties are defined. Also, without in-depth descriptions of the methods used for segmentation and reconstruction, validation studies cannot be reproduced. Previous studies have performed validations of aOCT airway size measurements against caliper or CT measurements in static phantoms [20], [22], [23], *ex vivo* pig airways [24], [25] and dynamic *in vivo* human airways [22], [23], [26]. Calipers can provide ground truth diameter measurements when phantom airways are geometrically simple, but in more representative phantoms diameters can be difficult to reproduce in aOCT due to different orientations and coordinate systems. In these cases CT was often the best option for the ground truth measurement of airway size. However, the lower spatial and temporal resolution of CT limits the assessment of the accuracy of aOCT to that of CT. Our alternate approach is to start with static, 3D printed samples as ground truth controls, and validate aOCT and CT airway size measurements independently, allowing us to compare the accuracy of each modality, similar to the work by Chen *et al.* [18] with multiple different CT scanners. This paper lays the groundwork for future CFD modeling and diagnostic examination of airway models constructed from aOCT scans as an alternative to CT by independently refining and validating the methods of segmentation, resampling, reconstruction, and geometric measurement of physical and virtual samples of well-characterized size and shape. Because of the relationship between airway size/shape and airflow resistance [27], we focused on quantification of airway cross-sectional area (CSA) as the primary figure of merit. This paper also provides detailed methods for aOCT 3D reconstruction, validated in non-trivial virtual samples, in addition to methods used for CT and 3D printed phantom airway measurements, for reproducibility. This effort culminates in estimates of the accuracy of both aOCT- and CT-derived 3D reconstructions of model airways from fine samplings of continuous cross-sections.

The first step in building accurate 3D models of airways from aOCT or CT scans was accurate segmentation of the airway lumen. CSA measurements derived from aOCT of simple cylindrical tubes were compared to ground-truth values from caliper measurements, as done in the past [22]–[24], [28]; here we used them to validate aOCT and develop CT segmentation methods. We then present a method to resample the helically-sampled aOCT data into Cartesian space for easy comparison with CT. To validate the resampling method, CSA measurements from simulated scans of virtual cones were compared against the model cone CSA. Lastly, a 3D printed model of a pediatric airway was used to validate the CT segmentation method, and the accuracy of 3D reconstructions

TABLE I
PEEK TUBE MEASUREMENT RESULTS

Tube Label	True CSA (mm²)	CT CSA (mm²)	CSAPR (mm²)	CSAPR Error (%)	rCSA (mm²)	rCSA Error (%)
A	27.48 ± 0.15	26.19 ±0.25	26.69 ± 0.34	-2.9	26.73 ± 0.31	-2.7
B	62.57 ± 0.21	61.65 ± 0.19	62.54 ± 0.36	-0.054	62.46 ± 0.28	-0.17
C	113.93 ± 0.41	112.40 ± 0.27	114.75 ± 0.67	0.72	113.38 ± 0.45	-0.48
D	177.97 ± 0.62	176.71 ±0.32	179.90 ± 0.48	1.1	178.81 ± 0.50	0.47
E	255.29 ± 0.49	254.23 ±0.39	260.3 ± 2.6	2.0	260.1 ± 1.7	1.9

True CSA based on caliper diameter measurements and calculated using (1).

of both CT and aOCT against the ground-truth stereolithography (STL) file used to print the model.

Because of the established wide use of CT throughout medical practice, it is expected that CT measurements will resemble true values very closely. aOCT measurements are hypothesized to provide similar accuracy as CT, and the methods developed here will guide future evaluation of endoscopic aOCT for airway imaging.

II. METHODS

A. Imaging Samples

The first set of samples consisted of 5 cylindrical tubes made of Polyether ether ketone (PEEK), each 50 mm long with inner diameters ranging 6mm to 18mm in increments of 3 mm. The tubes were machined instead of 3D printed, and their true size was measured using calipers. The diameter, d, of each tube was measured on each opening 6 times, each with different random orientations. The average and standard deviation of caliper diameter measurements, d and σ_d, respectively, were used to calculate true CSA and its uncertainty (by propagation of uncertainty with respect to d) (results in Table I in section III-C):

$$CSA_{True,PEEK} = (\pi/4)\, d^2, \quad \sigma_{CSA_{True,PEEK}} = (\pi/2)\, d\, |\sigma_d|. \quad (1)$$

The next type of sample was mathematically-modeled virtual cones used to validate the aOCT Cartesian resampling method. Ideal aOCT scans of the virtual cones were simulated, and data were treated similarly to real aOCT scans including segmentation, resampling, and measuring CSA. Simulated CSA measurements were then compared to the known true CSA from the virtual cone. The virtual cones provided a slightly more complex sample than PEEK tubes since cone CSA (in the *x-y* plane) changes with axial (*z*) position, according to:

$$CSA_{True,cone}(z) = \pi \tan^2(\alpha/2)(z-c)^2 \quad (2)$$

where α is the cone opening angle, and c is the axial position of the cone vertex.
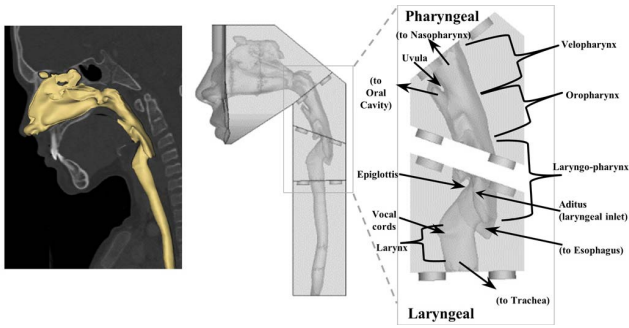
Fig. 1. Pediatric Airway Phantom. CT scan of pediatric patient (left) with the 3D reconstructed airway (yellow) overlaid. Complete pediatric airway model (middle). Phantom pharyngeal and laryngeal segments (right) in 3D housings were used to compare aOCT and CT.

The last type of sample, and the most complex, was two segments of a 3D printed pediatric airway phantom. CT and aOCT measurements of phantom CSA were compared to the ground-truth STL file that printed the phantom to validate CT segmentation and provide airway geometry accuracy metrics for each imaging modality. To create an airway phantom, a high-resolution CT scan, with pixel size of 0.471mm by 0.471 mm and slice increment 0.3 mm, of the upper airways of a 10-year-old male with normal airways was retrospectively obtained from medical records at UNC Hospitals under IRB approval and de-identified. An airway segmentation was created using Mimics™ (Materialise, Inc., Leuven, Belgium) from the high-resolution CT scan [24], and triangulated with sides averaging 1 mm to 1.5 mm long. Approximation of the airway segmentation by this triangulation blunted some sharp features from the original CT, causing length decreases on the order of 0.2 mm. The triangulation was exported in STL format and embedded in a 3D housing using ICEM-CFD™ (ANSYS, Inc., Canonsburg, PA). Two segments of the airway and their housing (the pharyngeal and laryngeal segments, Fig. 1) were re-triangulated with sides averaging 0.5 mm long and converted to STL format using ICEM-CFD™. These two segments include the regions of airway anatomy where OADs often occur such as OSA in the velopharynx and SGS in the larynx. The pharyngeal and laryngeal STL files were 3D printed with a build layer of 0.1016 mm (0.004 in) using SLArmor™ Nickel-NanoTool composite material with nickel plating (ProtoLabs, Inc., Raleigh, NC). The airway wall components of the STL files were then separated from the housing of the pharyngeal and laryngeal models and used for comparison with CT and aOCT segmentations as presented below.

B. CT Scanning

CT scans were performed at the Biomedical Research Imaging Center at University of North Carolina at Chapel Hill (UNC-CH) using a Siemens Biograph 64 mCT. Since none of the samples were tissue, patient safe radiation dosing was ignored to ensure spatial sampling as close to the axial resolution of aOCT (~0.026 mm) [25] as possible. The in-plane pixel sizes of CT scans were also heavily dependent on the field-of-view (FOV) parameter, so FOV was reduced to contain only the sample airways. The in-plane pixel sizes for

PEEK tube and airway phantom CT scans were 0.141 mm by 0.141 mm and 0.102 mm by 0.102 mm, respectively. CT scans were conducted with 80 kVp, 200 mAs, slice thickness = 0.6mm, pitch = 0.35, and reconstruction kernel B70S. The finest possible slice thickness was used to reduce partial volume effects. CT scans were saved in the form of Digital Imaging and Communications in Medicine (DICOM) image stacks in the axial (x-y) plane with the finest possible spacing in z between images of 0.6mm.

C. CT Segmentation of Lumen

Segmentation of the lumen from CT scans utilized the Canny edge detector [29], [30], and supervised airway edge selection with an interactive graphical user interface (GUI) written in Matlab (Mathworks, Inc.). Briefly, each CT image slice was input to the function *edge* with parameter "method" set to "Canny" and otherwise default values; each output consisted of a binary image of detected edge pixels. The output images were then directed into function *bwboundaries* [31] using default parameters to determine the objects (an object being a set of connected edge pixels) and their corresponding holes (a hole being a set of pixels fully enclosed by an object); the hole j within slice i is denoted as $A_{i,j}$. The problem was then to determine, for each slice i, which of the j holes ($A_{i,j}$) corresponded to the true lumen, denoted as A_i. Our solution was to manually select the correct hole from the first slice, then to automatically select the correct hole from adjacent slices based on similarity (overlap). This was implemented as follows: the first slice and its objects were overlaid within the GUI, the object corresponding to the air-tissue interface was manually selected, and its corresponding hole, A_1, was assigned as the true lumen for that slice. The correct holes from consecutive slices (A_2, A_3, etc.) were then assigned iteratively according to:

$$A_{i+1} = \min_j \left(A_i \oplus A_{i+1,j} \right)$$
$$= \min_j \left(\left(A_i - A_{i+1,j} \right) \cup \left(A_{i+1,j} - A_i \right) \right) \quad (3)$$

where the "exclusive or" operation was used to compute the number of non-overlapping pixels. The hole exhibiting the minimum non-overlap with the true lumen from the previous slice, then, was selected as the true lumen, allowing for propagation of the luminal volume from the first slice to the last slice. The final segmented airway lumen was saved in DICOM format. In rare cases where the method auto-selected the incorrect edge or edge detection failed, the user intervened with the GUI to manually force selection of one edge over another or draw the correct edge over the current slice.

D. CT Segmentation Development

The CT segmentation method above identifies the air-tissue interface and counts pixels contained within the interface as airway lumen. However, there is ambiguity regarding whether to include the segmented edge pixels as part of the airway for CSA measurement. To determine the most accurate way to handle these edge pixels, the CSA of PEEK tubes was initially calculated without, with half, and with all edge pixels from segmented CT scans. The best method, as shown in

section III-A below, was determined to be without edge pixels, which was then used to analyze all CT subsequent data.

E. aOCT Scanning

The aOCT system has been described in detail previously [24], [28]. Briefly, the system is comprised of a wavelength-swept laser source centered at 1310 nm with a sweeping range of 30 nm and rate of 5 kHz. A fiber-optic catheter delivered the sample arm light and was set up to scan luminal samples helically via simultaneously rotating and translating (pull-back). The primary difference with previous work was that an optical attenuator was added into the sample arm to avoid saturation caused by occasional specular reflections from the pediatric airway phantom. aOCT scans were performed with a pull-back speed, v, of 1 mm/s and rotation rate, f, of 10 Hz collecting 500 A-lines (axial-lines) per rotation over 25 mm of pull-back distance. The laser beam exiting the catheter was angled $\phi_{cath} = 75°$ from the catheter (z) axis (Fig. 2); this angle was chosen to reduce specular reflection from the protective sheath. A digital dispersion compensation algorithm based on entropy minimization was used when converting the aOCT raw (Fourier domain) data into image data [32], [33].

F. aOCT Segmentation of Lumen

A gradient-based automated segmentation algorithm utilizing wavelet filtering was performed as follows to locate the air-tissue interface throughout all A-lines of the scan. Since there was only air between the aOCT catheter and the airway wall, large increases in intensity with respect to distance from the aOCT catheter (intensity gradients) signified possible edges. Because aOCT noise is spatially dependent, a reference scan of only air was used to establish a noise level for initial thresholding of possible edges. Next, neighborhood filtering of 3 pixel $\times$ 3 pixel neighborhoods centered at all candidate edges was performed to reduce the number of candidate edge pixels in each A-line, following the assumption that the edge of the lumen should be continuous and near other edge pixels across consecutive A-lines. Then, the edge closest to the aOCT catheter in each A-line was selected and used to guide a shape-preserving piecewise cubic interpolation (*pchip* function in Matlab [34]) to fill in any remaining blank A-lines. As with CT, consecutive slices (or, in this case, rotations of the aOCT catheter) were assumed to be relatively similar in shape and size, so a median filter of each rotation with its neighbors was used to remove outliers. Finally, after smoothing with a moving average filter with window of 5 A-lines, the initial segmentation was overlaid on the aOCT image in a Matlab GUI for inspection and manual correction by a trained expert. Like with CT, the GUI enabled the inspector to interactively adjust aOCT image contrast, magnification, and centering to help find the lumen edge and draw any needed corrections to the auto-segmentation results.

G. aOCT 3D Resampling Into Cartesian Space

The helical scan pattern of aOCT provides a perspective of the airway that is determined by three parameters: the axial (z) position of the catheter, $z_{cath}(t) = v \cdot t$ (where v is
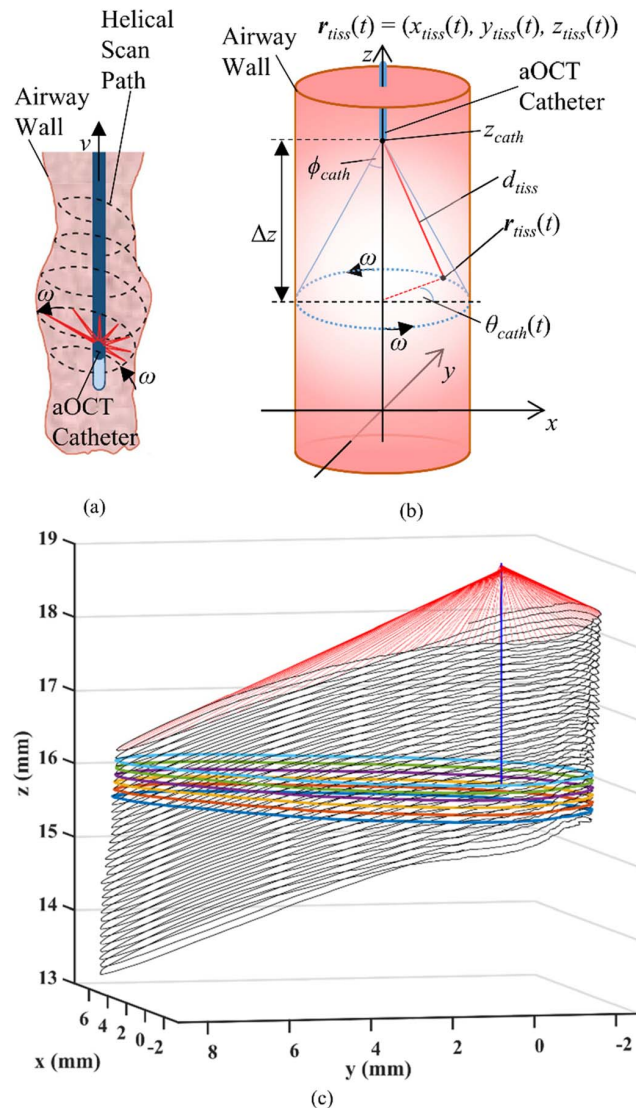

Fig. 2. (a) Illustration of aOCT helical scan with pull-back velocity v and angular velocity ω. (b) Geometric model of aOCT scanning when the catheter is stationary, $v = 0$, and centered along the axis of the cylindrical airway. (c) 3D Plot of the aOCT helical sampling (thin black) of laryngeal phantom; note how the off-center position of the catheter z_{cath} (blue vertical line) results in the line-of-sight tissue surface (red lines) to appear tilted relative to the x-y plane. The resampled cross-section polygons (thick assorted colors) are overlaid. Notice how any single resampled slice is reconstructed from multiple aOCT catheter rotations.

the pullback speed), the rotation (azimuthal) angle of the laser beam exiting the catheter, $\theta_{cath}(t) = \omega \cdot t$ (where $\omega = 2\pi/f$ is the angular velocity), and the fixed polar angle of the laser beam relative to the fiber optic (z) axis, ϕ_{cath}, as shown in Fig. 2. The aOCT system measures the line-of-sight distance from the catheter to the air-tissue interface, $d_{tiss}(t)$, which is the output of the lumen segmentation method described above. Our goal was to resample this segmentation into a binary Cartesian volume (a stack along z of binary x-y slices), like CT. This is non-trivial given the complexity of the scan pattern, as shown in Fig. 2, which depicts the helical aOCT sampling of laryngeal phantom overlaid with slices obtained by Cartesian resampling.

Cartesian resampling of $d_{tiss}(t)$ was performed as follows. The airway wall position illuminated by the laser at any point in time can be described in cylindrical coordinates as: $(r_{tiss}(t), \theta_{cath}(t), z_{tiss}(t))$. Since $\theta_{cath}(t)$ is already known, $d_{tiss}(t)$, $z_{cath}(t)$, and ϕ_{cath} were used to solve for missing parameters: $r_{tiss}(t)$ and $z_{tiss}(t)$. The difference between $z_{cath}(t)$ and $z_{tiss}(t)$ (denoted as $\Delta z(t)$) and $r_{tiss}(t)$ trace sides of a right triangle with hypotenuse $d_{tiss}(t)$ as shown in Fig. 2b, such that both can be solved for according to:

$$z_{tiss}(t) = z_{cath}(t) - \Delta z(t) = z_{cath}(t) - d_{tiss}(t)\cos(\phi_{cath})$$
$$r_{tiss}(t) = d_{tiss}(t)\sin(\phi_{cath}). \tag{4}$$

Given an integer number of A-lines per rotation, N, we used indices $i = 1 \ldots N$ to represent samples within a rotation, and $j = 1 \ldots J$ to represent the rotation number, where J is the total number of rotations in the scan. In this representation, the time-dependent parameters and data were then written as matrices $\theta_{cath}(i)$, $z_{tiss}(i, j)$, and $d_{tiss}(i, j)$.

The next step was to define the axial positions, $z(k)$, at which to interpolate the radial distance of the wall from the z axis, $r_{tiss}(i, k)$ while accounting for the non-perpendicular angle of the laser, ϕ_{cath}. The spacing between $z(k)$ positions was set equal to the aOCT scan pitch of 0.1 mm over a total of $k = 1 \ldots K$ slices. $r_{tiss}(i,k)$ was found by interpolating the surface of the airway wall in the axial direction, i.e., at each fixed catheter orientation i_0, $d_{tiss}(i_0,j)$ versus $z_{tiss}(i_0,j)$. We used *pchip*[34] to interpolate the line-of-sight distance $d_{tiss\_interp}(i_0,k)$ at each desired $z_{tiss} = z(k)$. We then converted each $d_{tiss\_interp}(i_0,k)$ value into a true radius $r_{tiss}(i_0,k)$ according to $r_{tiss}(i_0,k) = d_{tiss\_interp}(i_0,k) \cdot \sin(\phi_{cath})$; this process was then repeated for all catheter orientations $i_0 = 1 \ldots N$ to construct $r_{tiss}(i,k)$. Edge slice positions $z(k)$ that did not have r_{tiss} values for all N rotation angles were removed from the analysis.

Next, the interpolated results, $r_{tiss}(i,k)$, were converted to Cartesian coordinates, $x_{tiss}(i,k)$ and $y_{tiss}(i,k)$ according to $x_{tiss}(i,k) = r_{tiss}(i,k) \cdot \cos(\theta_{cath}(i))$, $y_{tiss}(i,k) = r_{tiss}(i,k) \cdot \sin(\theta_{cath}(i))$. The set of $N(x(i,k_0), y(i,k_0))$ coordinates in each slice k_0 were then used to represent vertices in a polygon tracing the shape of the airway lumen (see Fig. 2c). The Matlab function *roipoly* [35] was then used to compute masks of the airway lumen at a pixel sampling of 0.025 mm by 0.025 mm (in x and y), determined by the aOCT system's axial resolution. All other pixels were set equal to 0, providing a stack of equally spaced binary images in Cartesian coordinates to represent the segmented aOCT airway.

H. Simulated aOCT Scan

Simulated aOCT scans of mathematically modeled (virtual) cones were generated to validate the aOCT 3D resampling method above. These simulated scans were created by modeling the helical path traced by an aOCT scan, finding its intersection with the virtual cone surface, and solving for the line-of-sight distance $d_{tiss}(t)$. Fig. 3 illustrates the parameters used in the simulated scans.

Because of the angle ϕ_{cath} between the path of the laser and the catheter, the path traced by the aOCT scan can be
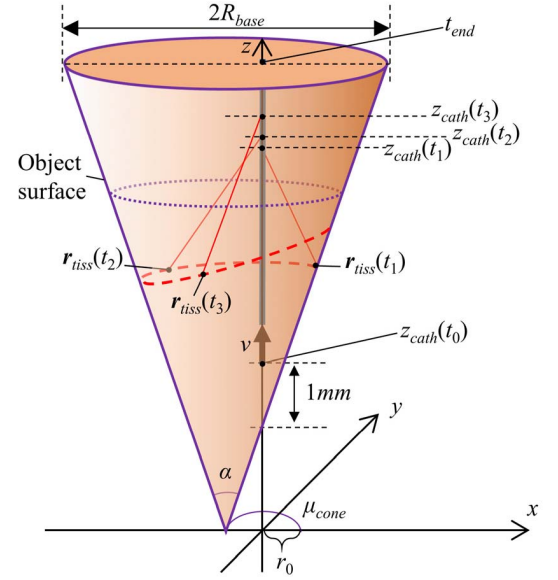

Fig. 3. Illustration of a simulated aOCT scan of a virtual cone. Note how the path the catheter starts, $z_{cath}(t_0)$, 1 mm away from where it intercepts the cone wall to ensure only the inside of the cone is scanned.

mathematically modeled like a cone centered on and moving along the z-axis with a constant opening angle of $2\phi_{cath}$ and a vertex located at $z_{cath}(t)$ described by the equation

$$x_{tiss}(t)^2 + y_{tiss}(t)^2 = \Delta z(t)^2 \tan^2(\phi_{cath}) . \tag{5}$$

The x and y components of the airway wall position, $x_{tiss}(t)$ and $y_{tiss}(t)$ respectively, can be described terms of $d_{tiss}(t)$ and $\theta_{cath}(t)$ as

$$x_{tiss}(t) = d_{tiss}(t)\cos(\theta_{cath}(t))\sin(\phi_{cath})$$
$$y_{tiss}(t) = d_{tiss}(t)\sin(\theta_{cath}(t))\sin(\phi_{cath}). \tag{6}$$

The virtual cones were modeled with axis symmetry in z, with vertex position $(r_0 \cdot \cos(\mu_{cone}), r_0 \cdot \sin(\mu_{cone}), c) = (a, b, c)$, where r_0 is the lateral displacement of the vertex from the catheter axis, μ_{cone} is the angle between the cone vertex and the positive x-axis, and with opening angle α. As such, the surface positions of the cones are subject to the relation:

$$(x_{cone} - a)^2 + (y_{cone} - b)^2 = (z_{cone} - c)^2 \tan^2(\alpha/2). \tag{7}$$

Our goal was then to solve for $d_{tiss}(t)$ when the scanning laser intersects the cone, i.e., when $(x_{tiss}(t), y_{tiss}(t), z_{tiss}(t)) = (x_{cone}, y_{cone}, z_{cone})$. Using (4)–(7) and simplifying the result yields a quadric equation for $d_{tiss}(t)$:

$$Ad_{tiss}(t)^2 + Bd_{tiss}(t) + C = 0$$
$$A = \cos^2(\phi_{cath})\left(\tan^2(\alpha/2) - \tan^2(\phi_{cath})\right)$$
$$B = 2r_0\sin(\phi_{cath})\cos(\theta_{cath}(t) - \mu_{cone})$$
$$\qquad + 2(c - z_{cath}(t))\cos(\phi_{cath})\tan^2(\alpha/2)$$
$$C = (z_{cath}(t) - c)^2\tan^2(\alpha/2) - r_0^2. \tag{8}$$

$d_{tiss}(t)$ was then computed for a simulated scan in $z_{cath}(t)$ with the starting position chosen to ensure $z_{cath}(t)$ was at least 1 mm from the intersection between the z axis and wall of the virtal cone. The ending position of the scan, $z_{cath}(t_{end})$,

TABLE II
aOCT VIRTUAL CONE SIMULATION RESULTS

r_0 (mm)	R_{base} (mm)	α (°)	z range (mm)	Mean CSA Difference (mm²)	STD CSA (mm²)
1	10	90.0	4.9	2.47×10^{-3}	6.0×10^{-3}
1	20	127	4.1	-1.85×10^{-2}	7.4×10^{-3}
1	15	113	4.5	3.98×10^{-3}	6.0×10^{-3}
1	5	53.1	5.5	4.78×10^{-3}	3.5×10^{-3}
2	10	90.0	4.5	-4.37×10^{-3}	5.0×10^{-3}
3	10	90.0	4.1	-1.58×10^{-2}	7.2×10^{-3}
4	10	90.0	3.7	-1.35×10^{-2}	5.2×10^{-3}
0	10	90.0	8.5	-3.36×10^{-3}	1.0×10^{-2}

was chosen such that the radial opening of the cone reached R_{base} (i.e., $z_{cath}(t_{end}) = c + \tan(\alpha/2)/R_{base}$). The temporal sampling was matched to that of the experimental conditions: $v = 1$ mm/s pull-back speed, $f = 10$ Hz rotation rate, and $N = 500$ A-lines per rotation to simulate $\theta_{cath}(t)$ and $z_{cath}(t)$. The simulation was performed on 8 different virtual cones all with varying R_{base} (5 mm to 20 mm), and r_0 (0 mm to 4 mm), resulting in varying total axial scan distances z_{range} (3.7 mm to 8.5 mm) as shown in Table II. All virtual cones had heights of 10 mm. Simulations used the same aOCT scan parameters as in the PEEK tube and airway phantom scans. After solving for $d_{tiss}(t)$ the result was read into the aOCT 3D resampling function, just like an actual scan, to obtain resampled slices with pixel size 0.025 mm by 0.025 mm (in x and y) and 0.1 mm spacing in z.

I. CSA Measurement for CT and aOCT

CSA was measured from segmented CT scans by multiplying the number of segmented airway pixels (not including edge pixels) in each slice by the pixel area. CSA for aOCT segmentations was calculated in two different ways. Like past experiments the CSA of each catheter rotation, CSA per rotation (CSAPR), was calculated by numerically integrating the radial distance to the airway wall over N A-lines [24]. The second method, resampled CSA (rCSA), was used to measure CSA from resampled aOCT slices and, like CT, consisted of multiplying the number of segmented airway pixels by the pixel area in each slice.

It is important to note that the PEEK tube CSA measurements were obtained via caliper measurements orthogonal to the long axis of each tube; However, when scanning there exists a slight tilt angle between the scan, z, axis and the long axis of the tube. This angle biases CSA measurements in both CT and aOCT scans, making the segmented tube slices appear as ellipses instead of circles. To determine and compensate for the tilt angle η, the movement of the center of mass (COM) of the airway was tracked as a function of z. The movement of the COM leads to the relation $\cos(\eta) = z/l$, where z is the z-distance between slices and l is the scalar 3D distance between COMs of slices. To convert the ellipse areas

back into their corresponding circular areas, we then used the relation $CSA = A_e \cdot \cos(\eta)$ [36] where A_e is the ellipse area as originally segmented from the tube scans. In this way, the tilt-compensated CSA from aOCT and CT could be compared to the caliper-measured CSA for PEEK tubes.

J. 3D Alignment and Co-Registration

For airway phantom scans, the stereolithography data (STL) was used to provide the ground truth CSA. Because the segmented stacks of CT and aOCT slices were oriented differently from each other and from the STL, it was necessary to align and co-register a copy of the STL to the CT and to the aOCT segmentations separately. Since both the 3D resampled aOCT scans and segmented CT scans were in Cartesian format, each binary image stack was readily imported into Materialise Mimics separately for alignment with the STL. First, the user utilized the Mimics GUI to coarsely align the STL airway to the scanned airway. Then, Mimics's automated alignment functions were used to further optimize the STL alignment to the scan and co-register the two to each other. In most cases the "STL Registration" function in Mimics was used. This function uses Powell's minimization method to minimize the distance between the point cloud rendering of STL and the masked airway. When this function failed to improve upon manual alignment, the "Global Registration" function, which utilizes an iterative closest point algorithm to minimize node-to-node distances between the STL and masked airway, was used instead.

After co-registration, the aligned STL was converted to a mask in Mimics and exported as a binary image stack with the same dimensions and orientation as the segmented aOCT or CT scan the STL was aligned to. Subsequently, a direct slice-to-slice comparison of the co-registered STL to its corresponding scan's cross-sections was performed by computing the CSAs at each slice. Furthermore, we examined the degree to which the shape of the segmented airways overlapped the STL within each slice by computing the percent non-overlap CSA (pnoCSA); this was defined as the number of airway pixels in the aOCT but not in the STL-derived airway, $\{p \in aOCT | p \notin STL\}$, divided by the total number of pixels in the STL airway. This was also done for the airway pixels in STL but not in aOCT $\{p \in STL | p \notin aOCT\}$, in STL but not CT $\{p \in STL | p \notin CT\}$, and in CT but not STL $\{p \in CT | p \notin STL\}$.

III. RESULTS

A. CT Segmentation Development

CT CSA measurements of PEEK tubes were compared against caliper measurements to develop the CT segmentation method. The CSA of each tube was calculated without, with half, and with all edge pixels, averaged over all slices, and the caliper CSA measurement was subtracted from the results to define the accuracy in CSA for each method. Fig. 4 illustrates the error in CSA measurement of each PEEK tube for all three methods. With the exception of PEEK tube A, CSA measurements were most accurate when the edge pixels were not used, and importantly, did not show any trend with true CSA, instead exhibiting a relatively constant negative bias
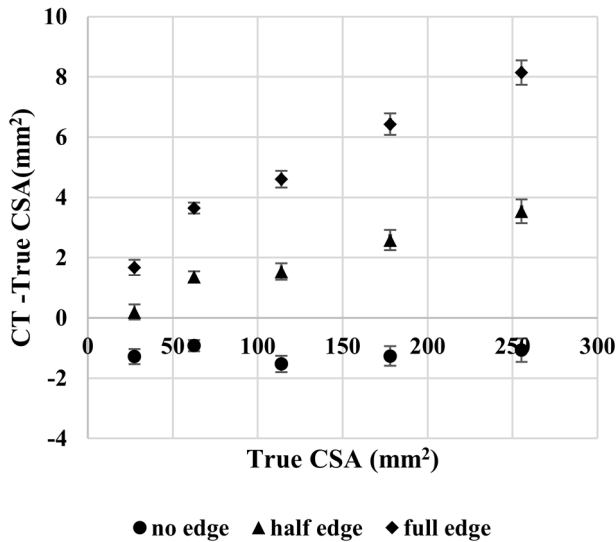
Fig. 4. Accuracy of CT segmentation methods in PEEK tubes of varying inner diameters, illustrated by plotting the difference between CSA obtained from CT and that from caliper measurements, versus the CSA of each tube. Vertical error bars indicate the standard deviation of CSA over all imaged slices, horizontal error bars (too small to be seen here) indicate propagated uncertainty for PEEK tube true CSA (see Table I).

of -1.21 ± 0.23 mm^2. When using half or all the edge pixels CSA measurements were less accurate, exhibiting an average bias of 1.8 ± 1.3 mm^2 and 4.9 ± 2.5 mm^2, respectively. Therefore, all CT segmentations excluded edge pixels in the following study. It is also notable that the standard deviations for the true and CT CSA for each tube are all of the same orders of magnitude (see Table I).

B. aOCT Segmentation Validation

Average CSAPR measurements (i.e., CSA obtained for each rotation of the aOCT catheter without Cartesian resampling) were used to validate the semi-automated aOCT segmentation method against caliper measurements of the PEEK tubes. Results are summarized in Table I. The CSAPR for all tubes was within $\pm$ 2.9% of true the CSA. CSAPR for tubes A, B, C, and D were all within 1.1mm^2 of true values and had standard deviations of the same order of magnitude as the caliper measurements. Tube E exhibited larger error in CSA of 5mm^2, and exhibited a standard deviation an order of magnitude higher than the true CSA uncertainty. The larger error in CSA for the largest tube is attributed to the difficulty in accurately segmenting edges located at larger distances from the aOCT catheter, due to the roll-off of the aOCT signal with distance. However, the error in CSA is still within 2% of the true value for tube E.

C. aOCT Resampling Validation

To test the hypothesis that rCSA measurements of the PEEK tubes agree with CSAPR, the aOCT PEEK tube segmentations from the previous section were resampled into 3D Cartesian space. Results can be found along with the corresponding CSAPR measurements in Table I. As expected, rCSA measurements were consistent with CSAPR within one standard deviation, confirming the hypothesis. This comparison,
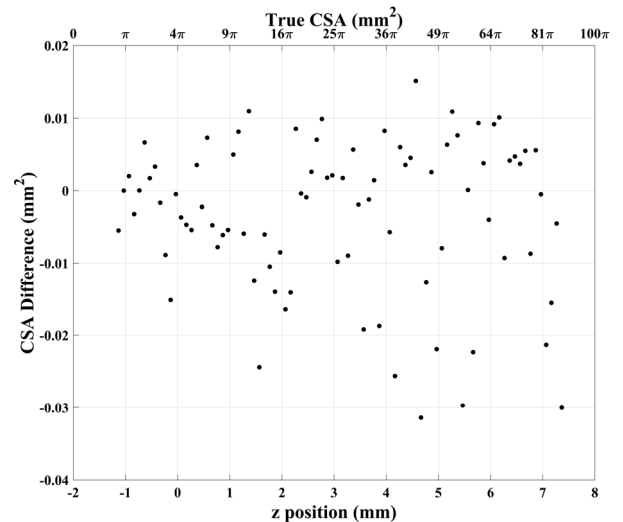

Fig. 5. Characteristic plot of the difference between rCSA and true CSA for a virtual cone simulation. The difference in CSA values is random with respect to true CSA.

however, only applies for samples like the PEEK tubes in which CSA is constant along length.

To address this limitation, simulated scans of virtual cones were used to validate the aOCT 3D resampling method by comparing the CSA of the virtual model against rCSA at multiple slices. Table II summarizes virtual cone parameters and results of each simulation. As expected, rCSA agreed well with true CSA for all cone models with the largest absolute average rCSA error of less than 2×10^{-2}mm^2. In comparison to the errors obtained in the PEEK tube measurements, this suggests that any error caused by resampling would be negligible. Fig. 5 contains a characteristic plot of rCSA error against slice position and true CSA from the simulation in the bottom row of Table II. As expected, the estimated values are evenly distributed around the true values and do not exhibit bias as the CSA gets larger across the cone.

D. Validation of CT and aOCT Against STL in 3D Printed Phantom

Each scan (CT or aOCT) of phantom airway geometry was compared to its co-registered STL via direct slice-by-slice CSA analysis. This consisted of calculating the CSA of each segmented slice in the stack and its 3D co-registered STL counterpart. Plots of results for CT and aOCT are paired with Mimics 3D visualizations and representative cross-sections in Fig. 6 and Fig. 7. Over all slices, the mean CSA difference between STL and CT for the pharyngeal and laryngeal segments were -5.5 ± 4.9 mm^2 and -2.1 ± 1.2 mm^2 respectively. When the STL is compared to the aOCT, however, the mean CSA difference is -3.8 ± 10.0 mm^2 and -19 ± 39 mm^2 for pharyngeal and laryngeal segments respectively. The laryngeal especially highlights that like endoscopy, aOCT suffers from line-of-sight limitations. Fig. 6d and Fig. 7d show how in the laryngeal segment aOCT completely misses regions near the epiglottis and laryngo-pharynx in the z range of 0.1 mm to 4.8 mm. To a lesser extent, the same is true of the pharyngeal segment in the z range 0.1 mm to 4.9 mm
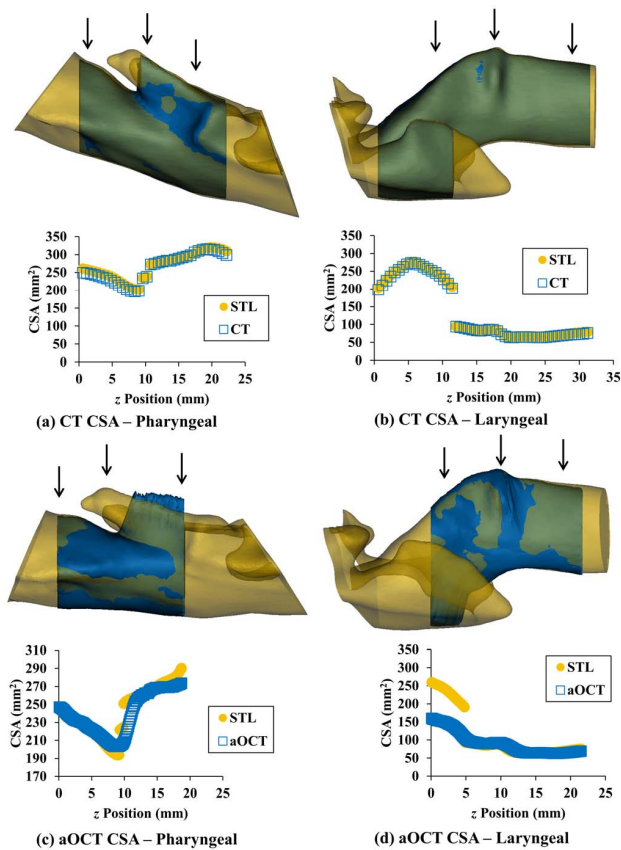
Fig. 6. CT vs STL (a and b) and aOCT vs STL (c and d). Mimics 3D reconstructions of scans are overlaid on aligned STL counterparts and above slice-by-slice CSA plots for each airway segment. Arrows above 3D reconstructions denote positions of example cross sections in Fig. 7.
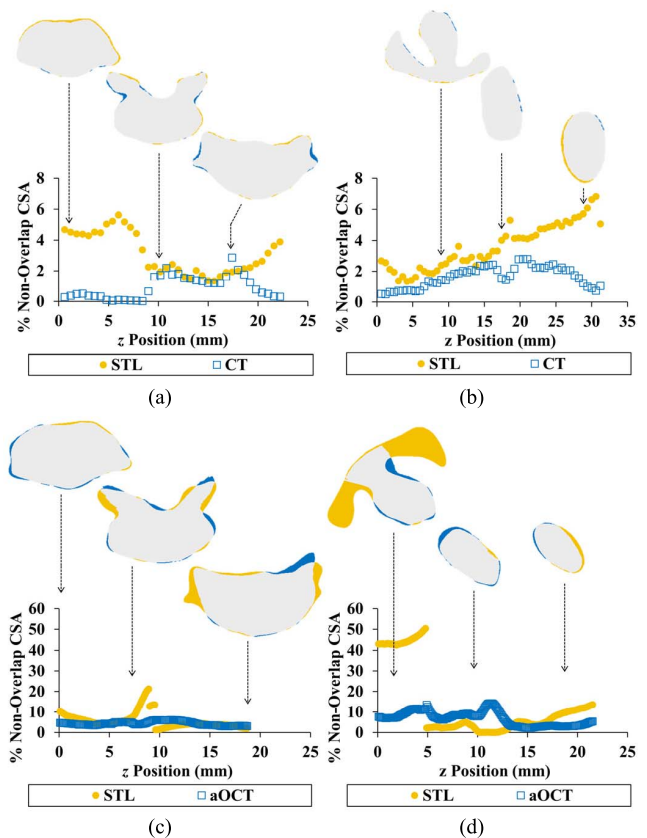

Fig. 7. Percent non-overlap CSA. Representative cross-sections illustrate accuracy in measured airway shape above pnoCSA plots. Gray regions correspond to scan and STL pixels that overlap while yellow regions are STL non-overlap pixels and blue regions are scan non-overlap pixels. (a) CT pnoCSA–Pharyngeal. (b) CT pnoCSA–Laryngeal. (c) aOCT pnoCSA–Pharyngeal. (d) aOCT pnoCSA–Laryngeal.

near the velopharynx and oropharynx where regions were partially obstructed. Knowing this, the mean CSA difference between STL and aOCT was calculated for unobstructed regions, resulting in $2.2 \pm 3.5 mm^2$ and $1.5 \pm 5.3 mm^2$ for pharyngeal and laryngeal segments respectively. For comparison, the mean CSA difference between STL and CT in similar regions of the pharyngeal and laryngeal segments are $-3.4 \pm 4.3 mm^2$ and $-1.9 \pm 1.2 mm^2$. As such, we conclude that the ground-truth error in CSA for unobstructed regions is of similar magnitude when using aOCT or CT. Results of these comparisons in obstructed and unobstructed regions are summarized in Table III.

While the mean CSA difference is a good measure of the accuracy of the airway size for aOCT and CT, it doesn't give much information about the accuracy of the airway *shape* against the ground-truth STL. To quantify accuracy in airway shape, percent non-overlap CSA (pnoCSA) was measured from the aOCT and CT scans of both airway phantoms. Slices whose aOCT or CT airway completely agreed with the STL shape would have 0% non-overlap CSA (pnoCSA) in both the scan and STL metrics. Slices where the STL or scan pnoCSA were large corresponded to inaccuracies in the measured airway shape. Fig. 7 provides plots of pnoCSA against slice position along with representative cross-sections for both aOCT and CT of the pharyngeal and laryngeal segments. These plots can help quantify the previously mentioned line-of-sight

TABLE III
aOCT AND CT AIRWAY PHANTOM ACCURACY COMPARISON

Scan vs STL	CT	aOCT	CT	aOCT	CT	aOCT	CT	aOCT
Phantom Segment	P	P	P uob	P uob	L	L	L uob	L uob
Slices	37	187	14	90	52	215	32	165
Z length (mm)	21.6	18.6	7.8	8.9	30.6	21.4	18.6	16.4
Mean CSA Difference (mm²)	-5.51	-3.77	-3.39	2.17	-2.14	-18.9	-1.86	1.49
STD CSA Difference (mm²)	4.87	9.95	4.31	3.50	1.18	38.6	1.19	5.30

uob = unobstructed region, P = pharyngeal, L = laryngeal,
STD CSA Difference = standard deviation of CSA difference across all slices.

limitations in aOCT in regions where the STL pnoCSA is significantly larger than the aOCT pnoCSA (e.g., $z = 0$ mm to 5 mm on the laryngeal segment, Fig. 7d). On the other hand, regions where the aOCT pnoCSA is larger correspond to slices where the aOCT airway shape doesn't agree well with the STL. While the CT pnoCSA for both pharyngeal and laryngeal segments was generally smaller than the STL pnoCSA, the small magnitude in comparison to aOCT suggests the error is not due to obstructed view, but alignment.

IV. DISCUSSION

As expected, both CT and aOCT measurements in PEEK tubes agreed with caliper measurements. This is consistent with previously published works using tubes for validation of aOCT CSA [22]–[24], [28]. In both scanning methods, percent CSA difference for tube A was greatest, which is attributed to the fact that tube A was the smallest, thus CSA differences comprised a larger fraction of the total CSA. In CT PEEK tube CSAs were slightly underestimated when using the "no edge" method, and largely overestimated when using the "full edge" method, which lead to our choice of excluding edge pixels from further analysis. However, it is important to note that there are methods for modeling the X-ray attenuation signals in pixels containing multiple constituent materials, i.e., the partial volume effect, that can further improve accuracy. Partial volume corrections have been developed in many CT applications to provided sub-voxel spatial information [37], [38]. Correction methods similar to [38] may shift the bias in CSA compared to our "no edge" CT method by 1 to 2 mm^2, however, a more detailed development is needed in the future to model and employ partial volume corrections specifically for estimating lumen CSA. There also is a possible trend of aOCT where CSAPR bias increases with CSA, however, this trend is not observed for rCSA in the PEEK tubes. Importantly, the data suggest that CSAPR, which is calculated based on catheter rotations in the helical space, is generally less accurate than rCSA, which is computed within the Cartesian resampled airway volume. Also as expected, the rCSA measurements from simulated aOCT scans of virtual cones were very accurate, within less than 1% of true CSA for all positions in all cones, validating the 3D resampling and rCSA measurement method in idealized conditions.

Interestingly, the error in rCSA for the simulated cones was significantly smaller, 1 to 3 orders of magnitude, than that of rCSA in PEEK tubes. We attribute these differences to two sources of error in experimental scans: non-uniform rotational distortion (NURD), and the assumed path of the catheter. NURD is a common issue in catheter-based systems, where variations in rotation rate throughout each rotational period are not accounted for and cause distortions in 2- or 3-D reconstructions. NURD is caused by mechanical friction and bends in the catheter [28], [39]. In this study, to reduce the effects of NURD, the catheter was mounted onto the optics bench where it was held straight and level while still allowing for the rotational and translational movement of the catheter. Variations in the pull-back path of the catheter from a straight line similarly caused issues with 3D resampling. We observed small but significant oscillations of the catheter tip about the transverse axis during scanning.

Like endoscopy, because of the catheter position dependent perspective provided by aOCT, scans of larger sections of the airway often require additional catheter position-tracking [20] to account for the natural airway curvature when creating 3D reconstructions. Some groups have accomplished this using additional CT and MRI scans [16], [40], but this defeats the purpose of using aOCT as an alternative to CT and MRI. In this study the problem was avoided by scanning over smaller distances and orienting the imaging samples so that the aOCT catheter could easily move in a straight path.

Unobstructed full reconstruction of much of the upper airway was possible via aOCT with only frames surrounding pockets or branches off the main airway, like the uvula, esophagus, and epiglottis, suffering from obstructed line-of-sight. Being endoscopically deployed, aOCT has the same obstructed view limitations as video endoscopy, while providing better quantitative measurements. Like in gold-standard endoscopy, obstructed regions can be distinguished in aOCT images by sharp discontinuities in the airway surface curve. As shown in Fig. 6 and 7, obstructions only take up a fraction of any given frame, with the rest consisting of reliable, unobstructed measurements. As shown in other aOCT studies, even with line-of-sight limitations, CFD simulations built from aOCT reconstructions can distinguish between diseased / healthy [1] and treated / untreated cohorts [41].

In the 3D printed phantom, CT CSA measurements of both segments closely matched true values. This, combined with the small values of pnoCSA, validates the semi-automated airway segmentation method used for CT scans. The CSA vs position plots in Fig. 6 and 7 underscore the novelty of this validation method for 3D reconstruction from continuous cross-sections. This is important for future *in vivo* experiments employing CT scans for ground-truth validation of aOCT. Other studies have compared aOCT to CT [22], [23], [25], [26], however unlike those studies, we provide detailed methods for segmenting CT images to aid reproducibility. Also, our work, unlike other studies, quantifies uncertainty in CT segmentations via comparison against ground truth STL geometries. This is important because CT segmentations suffer documented bias that stems from a lack of standardization of CT scanners, scan protocols, and image reconstruction methods [18]. In Fig. 7b, the monotonic increase in pnoCSA vs. position may suggest a slight alignment error, as STL and CT non-overlapping pixels only appear on opposite edges of the slices. As stated earlier, the Mimics alignment function that worked best was used to align the STL to the stack of CT (or aOCT) binary images. Tests showed that the same alignment functions worked differently when the slices in the stack were blurred. Future alignments of CT to aOCT may benefit from being treated as a triangulation of a point cloud, like in CFD, instead of a stack of slices. Because of the different sampling rates and image resolutions, it wasn't possible to directly align the slice stack of CT to aOCT in Mimics, however, a triangulation won't have this limitation. Another possible cause for discrepancies between the CT segmented phantom and the STL is unaccounted partial volume effects. While the "no edge" method was sufficient in the PEEK tubes, the phantom is far more complex in shape and material. Future work is needed to establish a method to correct for these partial volume effects.

Both CT and aOCT scans were affected by the metallic surface of the airway phantom. We chose the metallic 3D printing material because it was robust to temperature changes, and could be reasonably imaged by both aOCT and CT. However the material also posed some limitations.

For aOCT the metallic surface can increase the effects of specular reflection and cause images to be bright and saturated at certain angles. After preliminary tests, an attenuator was added to the aOCT system to reduce sample power and edge saturation in scans. The metallic phantom introduced CT image artifacts like streaking, shading, and partial volume effects. The finest possible slice thickness was used to reduce partial volume effects. The GUI developed for both aOCT and CT allowed interactive contrast adjustment to help the inspector compensate for saturating, streaking and shading artifacts and correct auto-segmentation when needed. Future work may explore newer phantom materials that better mimic human airways. Another factor affecting aOCT measurements of the airway phantom is the depth dependence of the transverse resolution and signal-to-noise ratio (SNR). As distance from the catheter increased, both the noise in the image and the size of the physical space sampled by the laser increased as well. This caused edges to be faint, making it more difficult to accurately detect and segment the airway wall when it was farther away from the catheter. Also, because of the rotation of the catheter, for any arbitrary pair of consecutive A-lines the physical distance between pixels of the same optical depth was dependent on depth. All these factors combined resulted in less precision as the airway wall moved farther away from the catheter.

Eventual applications of this work include diagnostic examination of airways and CFD modeling to characterize disease states and predict patient treatment outcomes. While endoscopy and CT imaging are currently the gold-standard methodologies for these applications, lack of quantification and exposure to radiation severely limit these methods for extensive use. The present study demonstrates conditions under which aOCT imaging accuracy is similar to that of CT, and underscores several advantages of aOCT imaging over these methods. In particular, the resolution of aOCT imaging is considerably higher than CT. We note that existing methods for estimating partial-volume effects may be used to provide more accurate lumen measurements in CT [38]. In practice CT resolution is often lower than that of the scans employed here, especially when imaging a large region such as the respiratory tract or when imaging children, in order to keep radiation dose at a minimum. Low resolution contributes to inaccurate reconstructions containing "lumpy" or ridged surfaces. Surface roughness caused by low CT resolution can cause over-prediction of airway resistance in both CFD and physical models due to high pressure drops from the increased drag effects of wall friction [42], [43]. The higher resolution of aOCT imaging can provide smoother reconstructions of airway surfaces that avoid these limitations. In addition, aOCT scans can provide dynamic airway data [4], [12], [13] without radiation exposure. Such data are needed to characterize soft-tissue changes for the development of fluid-structure interaction models [44] that can predict airway wall collapse and assess potential treatment outcomes. Future work plans to build on the presented validation in static samples to quantify uncertainty in dynamic samples. The elimination of radiation exposure, while rapidly obtaining high-fidelity scans suitable for 3D reconstruction and CFD modeling of the airways is

especially significant for imaging in children, and the potential for aOCT imaging to expand research in areas such as pediatric OSA is compelling.

V. Conclusion

We performed an in-depth validation study of the methods used to measure the airway geometry from aOCT and CT scans by CSA measurement of well-characterized samples. Accurate measurements of the size and shape of the airway lumen can aid in diagnosis, treatment, and CFD simulation of obstructive airway disorders. It is believed that aOCT can provide measurements just as accurate as CT but faster and without exposure to harmful radiation over small scanning distances $\sim$25 mm; further development is needed for tracking the aOCT catheter tip position over larger distances. As expected, both methods measured the CSA of simple PEEK tubes with small amounts of error, often less than 2 mm^2. Simulated aOCT scans of virtual cones confirmed the method of resampling aOCT data into 3D Cartesian coordinates and analysis of CSA within image cross-sections (slices) analogous to CT images. The more complex pediatric airway phantoms highlighted the line-of-sight limitation of aOCT, however in unobstructed regions of both phantom segments the aOCT measurements of CSA were more accurate than those of CT. These results, combined with the wide use of endoscopy in airway inspection, emphasize endoscopic aOCT's viability as a fast, minimally-invasive, and accurate method for quantitative airway size and shape measurements.

References

[1] J. Cisonni *et al.*, "Effect of the velopharynx on intraluminal pressures in reconstructed pharynges derived from individuals with and without sleep apnea," *J. Biomech.*, vol. 46, no. 14, pp. 2504–2512, Sep. 2013.

[2] D. M. Wootton *et al.*, "Computational fluid dynamics upper airway effective compliance, critical closing pressure, and obstructive sleep apnea severity in obese adolescent girls," *J. Appl. Physiol.*, vol. 121, no. 4, pp. 925–931, Oct. 2016.

[3] G. K. Sharma *et al.*, "Long-range optical coherence tomography of the neonatal upper airway for early diagnosis of intubation-related subglottic injury," *Amer. J. Respiratory Critical Care Med.*, vol. 192, no. 12, pp. 1504–1513, Dec. 2015.

[4] A. M. D. Lee *et al.*, "Validation of airway wall measurements by optical coherence tomography in porcine airways," *PLoS ONE*, vol. 9, no. 6, p. e100145, Jun. 2014.

[5] D. C. Adams *et al.*, "Birefringence microscopy platform for assessing airway smooth muscle structure and function *in vivo*," *Sci. Transl. Med.*, vol. 8, no. 359, pp. 131–359, Oct. 2016.

[6] T. L. Wakefield, D. J. Lam, and S. L. Ishman, "Sleep apnea and sleep disorders," in *Cummings Otolaryngology*, 6th ed. Philadelphia, PA, USA: Elsevier, 2015, pp. 252–270.

[7] G. H. Zalzal and R. T. Cotton, "Glottic and subglottic stenosis," in *Cummings Otolaryngology*, 6th ed. Amsterdam, The Netherlands: Elsevier, 2015, pp. 3158–3170.

[8] H. H. Patel, D. Goldenberg, and J. D. McGinn, "Surgical management of upper airway stenosis," in *Cummings Otolaryngology*, 6th ed. Amsterdam, The Netherlands: Elsevier, 2015, pp. 982–992.

[9] M. Slaats *et al.*, "Predicting the effect of treatment in paediatric OSA by clinical examination and functional respiratory imaging," *Pediatric Pulmonol.*, vol. 52, no. 6, pp. 799–805, Jun. 2017.

[10] F. Mahmood and N. J. Durr, "Deep learning and conditional random fields-based depth estimation and topographical reconstruction from conventional endoscopy," *Med. Image Anal.*, vol. 48, pp. 230–243, Aug. 2018.

[11] M. Visentini-Scarzanella, T. Sugiura, T. Kaneko, and S. Koto, "Deep monocular 3D reconstruction for assisted navigation in bronchoscopy," *Int. J. Comput. Assist. Radiol. Surg.*, vol. 12, no. 7, pp. 1089–1099, 2017.

[12] R. A. McLaughlin *et al.*, "Static and dynamic imaging of alveoli using optical coherence tomography needle probes," *J. Appl. Physiol.*, vol. 113, no. 6, pp. 967–974, Sep. 2012.

[13] S. S. Hwang *et al.*, "*In vivo* real-time imaging of airway dynamics during bronchial challenge test," *Lasers Surg. Med.*, vol. 47, no. 3, pp. 252–256, Mar. 2015.

[14] V. Volgger *et al.*, "Long-range Fourier domain optical coherence tomography of the pediatric subglottis," *Int. J. Pediatric Otorhinolaryngol.*, vol. 79, no. 2, pp. 119–126, Feb. 2015.

[15] C. A. Coughlan *et al.*, "*In vivo* cross-sectional imaging of the phonating larynx using long-range Doppler optical coherence tomography," *Sci. Rep.*, vol. 6, no. 1, Sep. 2016, Art. no. 22792.

[16] F. B. Lazarow *et al.*, "Intraoperative long range optical coherence tomography as a novel method of imaging the pediatric upper airway before and after adenotonsillectomy," *Int. J. Pediatric Otorhinolaryngol.*, vol. 79, no. 1, pp. 63–70, Jan. 2015.

[17] M. Kirby, W. Zhang, P. K. Laratta, D. D. Sin, S. Lam, and H. O. Coxson, "Sex differences in chronic obstructive pulmonary disease evaluated using optical coherence tomography," *Proc. SPIE*, vol. 8927, p. 89270Z, Mar. 2014.

[18] H. Chen *et al.*, "Accuracy of MDCT and CBCT in three-dimensional evaluation of the oropharynx morphology," *Eur. J. Orthodontics*, vol. 40, no. 1, pp. 58–64, Jan. 2018.

[19] H. E. Calloway *et al.*, "Comparison of endoscopic versus 3D CT derived airway measurements," *Laryngoscope*, vol. 123, no. 9, pp. 2136–2141, Sep. 2013.

[20] B. Lau, R. A. McLaughlin, A. Curatolo, R. W. Kirk, D. K. Gerstmann, and D. D. Sampson, "Imaging true 3D endoscopic anatomy by incorporating magnetic tracking with optical coherence tomography: Proof-of-principle for airways," *Opt. Express*, vol. 18, no. 26, pp. 27173–27180, Dec. 2010.

[21] A. C. Loy *et al.*, "Anatomic optical coherence tomography of upper airways," in *Optical Coherence Tomography*. Cham, Switzerland: Springer, 2015, pp. 2245–2262.

[22] J. P. Williamson *et al.*, "Measuring airway dimensions during bronchoscopy using anatomical optical coherence tomography," *Eur. Respiratory J.*, vol. 35, no. 1, pp. 34–41, Jan. 2010.

[23] J. J. Armstrong, M. S. Leigh, D. D. Sampson, J. H. Walsh, D. R. Hillman, and P. R. Eastwood, "Quantitative upper airway imaging with anatomical optical coherence tomography," *Amer. J. Respiratory Critical Care Med.*, vol. 173, no. 2, pp. 226–233, Jan. 2006.

[24] K. Wijesundara, C. Zdanski, J. Kimbell, H. Price, N. Iftimia, and A. L. Oldenburg, "Quantitative upper airway endoscopy with swept-source anatomical optical coherence tomography," *Biomed. Opt. Express*, vol. 5, no. 3, pp. 788–799, Mar. 2014.

[25] R. Bu, H. Price, S. Mitran, C. Zdanski, and A. L. Oldenburg, "Swept-source anatomic optical coherence elastography of porcine trachea," *Proc. SPIE*, vol. 9689, p. 968923, Mar. 2016.

[26] R. A. McLaughlin *et al.*, "Applying anatomical optical coherence tomography to quantitative 3D imaging of the lower airway," *Opt. Express*, vol. 16, no. 22, pp. 17521–17529, Oct. 2008.

[27] S. C. Persak, S. Sin, J. M. McDonough, R. Arens, and D. M. Wootton, "Noninvasive estimation of pharyngeal airway resistance and compliance in children based on volume-gated dynamic MRI and computational fluid dynamics," *J. Appl. Physiol.*, vol. 111, no. 6, pp. 1819–1827, Dec. 2011.

[28] R. Bu, S. Balakrishnan, N. Iftimia, H. Price, C. Zdanski, and A. L. Oldenburg, "Airway compliance measured by anatomic optical coherence tomography," *Biomed. Opt. Express*, vol. 8, no. 4, pp. 2195–2209, Apr. 2017.

[29] J. Canny, "A computational approach to edge detection," *IEEE Trans. Pattern Anal. Mach. Intell.*, vol. PAMI-8, no. 6, pp. 679–698, Nov. 1986.

[30] *Find Edges in Intensity Image—MATLAB Edge, MATLAB Image Processing Toolbox Documentation*. Accessed: Jun. 22, 2017. [Online]. Available: https://www.mathworks.com/help/images/ref/edge.html

[31] *Trace Region Boundaries in Binary Image—MATLAB Bwboundaries, Documentation, MATLAB Image Processing Toolbox*. Accessed: Aug. 13, 2018. [Online]. Available: https://www.mathworks.com/help/images/ref/bwboundaries.html

[32] K. C. Wijesundara, N. V. Iftimia, and A. L. Oldenburg, "Design of a swept-source, anatomical OCT system for pediatric bronchoscopy," *Proc. SPIE*, vol. 8571, p. 85713K, Mar. 2013.

[33] D. L. Marks, A. L. Oldenburg, J. J. Reynolds, and S. A. Boppart, "Autofocus algorithm for dispersion correction in optical coherence tomography," *Appl. Opt.*, vol. 42, no. 16, pp. 3038–3046, Jun. 2003.

[34] *Piecewise Cubic Hermite Interpolating Polynomial (PCHIP)—MATLAB PCHIP, MATLAB Documentation*. Accessed: Dec. 15, 2017. [Online]. Available: https://www.mathworks.com/help/matlab/ref/pchip.html#bvjbz1m-2

[35] *Specify Polygonal Region of Interest (ROI)—MATLAB Roipoly, MATLAB Image Processing Toolbox Documentation*. Accessed: Jan. 9, 2018. [Online]. Available: https://www.mathworks.com/help/images/ref/roipoly.html

[36] E. W. Weisstein. *Cylindrical Segment*. Accessed: Sep. 6, 2017. [Online]. Available: http://mathworld.wolfram.com/CylindricalSegment.html

[37] F. Heckel *et al.*, "Segmentation-based partial volume correction for volume estimation of solid lesions in CT," *IEEE Trans. Med. Imag.*, vol. 33, no. 2, pp. 462–480, Feb. 2014.

[38] S. H. Conradi, B. A. Lutey, J. J. Atkinson, W. Wang, R. M. Senior, and D. S. Gierada, "Measuring small airways in transverse CT images: Correction for partial volume averaging and airway tilt," *Acad. Radiol.*, vol. 17, no. 12, pp. 1525–1534, Dec. 2010.

[39] O. O. Ahsen *et al.*, "Correction of rotational distortion for catheter-based *en face* OCT and OCT angiography," *Opt. Lett.*, vol. 39, no. 20, pp. 5973–5976, Oct. 2014.

[40] A. D. Lucey *et al.*, "Measurement, reconstruction, and flow-field computation of the human pharynx with application to sleep apnea," *IEEE Trans. Biomed. Eng.*, vol. 57, no. 10, pp. 2535–2548, Oct. 2010.

[41] J. S. Kimbell *et al.*, "Upper airway reconstruction using long-range optical coherence tomography: Effects of airway curvature on airflow resistance," *Lasers Surg. Med.*, Jul. 2018.

[42] J. T. Kelly, B. Asgharian, J. S. Kimbell, and B. A. Wong, "Particle deposition in human nasal airway replicas manufactured by different methods. Part I: Inertial regime particles," *Aerosol Sci. Technol.*, vol. 38, no. 11, pp. 1063–1071, Nov. 2004.

[43] J. D. Schroeter, G. J. M. Garcia, and J. S. Kimbell, "Effects of surface smoothness on inertial particle deposition in human nasal models," *J. Aerosol Sci.*, vol. 42, no. 1, pp. 52–63, Jan. 2011.

[44] J. Pirnar, L. Dolenc-Grošelj, I. Fajdiga, and I. Žun, "Computational fluid-structure interaction simulation of airflow in the human upper airway," *J. Biomech.*, vol. 48, no. 13, pp. 3685–3691, Oct. 2015.